In situ holograms and two-wave mixing amplification of conical diffraction vector waves

Muhammad Waqar Iqbal, Yuliia Shiposh, Anton Kohutych, Nicolas Marsal, Alexander Grabar, Germano Montemezzani

begindocument/before

In-situ holograms and two-wave mixing amplification of conical diffraction vector waves

MUHAMMAD WAQAR IQBAL,[1,2,*] YULIIA SHIPOSH,[3], ANTON KOHUTYCH,[3], NICOLAS MARSAL,[1,2] ALEXANDER A. GRABAR,[3] AND GERMANO MONTEMEZZANI[1,2]

[1] *Université de Lorraine, CentraleSupélec, LMOPS, 57000 Metz, France*
[2] *Chair in Photonics, CentraleSupélec, LMOPS, 57000 Metz, France*
[3] *Inst. for Solid State Physics and Chemistry, Uzhhorod National University, 88000 Uzhhorod, Ukraine*
[*] *muhammad-waqar.iqbal@univ-lorraine.fr*

Abstract: Holographic recording and selective reconstruction and amplification of conical diffraction vector waves is demonstrated using a nonlinear photorefractive $Sn_2P_2S_6$ crystal acting simultaneously as medium producing the conical diffraction effect and as holographic storage material. It is shown that upon propagation of the object wave along one of the optical axes of the biaxial crystal, the azimuthal spreading of the local linear polarizations across the conical diffraction ring allows its holographic recording with any combinations of the object and reference wave's input polarizations, including mutually orthogonal ones. We discuss the dependence of the recording and read-out polarizations on the recovered and amplified patterns and provide a simplified model qualitatively accounting for all the main observed features. The approach permits a tailoring of the reconstructed or amplified vector waves in terms of intensity and polarization distributions and opens interesting perspectives for their static or dynamic manipulation.

1. Introduction

Internal conical diffraction (CD) is a natural optical effect that produces specific types of vector beams having a spatially-dependent polarization. This phenomenon is observable upon propagation of a focused beam along one of the optic axes of an optically biaxial crystal (BC) and gives rise to a slanted cone with circular base [1–3]. The latter represents the locus of the Poynting vectors associated to the wavevector propagation along the singular direction of the optic axis. Even for a homogeneously polarized input wave, different linear polarizations are found to spread azimuthally across the ring section of the cone. Despite a nearly 200 years history since Hamilton's prediction [4], this phenomenon has seen a renewed interest in the last two decades. This has been enabled by a deeper theoretical understanding owing to a paraxial diffraction theory describing the CD vector waves [1, 5] and is motivated by both fundamental and applied aspects. In this context we may cite the interesting orbital angular momentum characteristics [6–10] and the new features allowed by novel configurations with a series of BC in cascade [11–15] that open new venues for the complex shaping of these vector beams, up to the case where the CD beams no longer possess the usual circular symmetry [16, 17]. Potential and recently demonstrated applications of CD include optical trapping of particles or Bose-Einstein condensates [18–20], free-space multiplexing for communication [21], beam shaping [15, 16, 22], polarimetry [9, 23, 24] or super-resolution imaging [25, 26].

Conical diffraction is a manifestation of the linear optical properties of the crystal and the above mentioned investigations have all been performed in the linear regime with the BC acting as passive elements. Nevertheless, few studies have combined CD with nonlinear optics, where CD at the second-harmonic wavelength [27–29] or at the sum-frequency generation wavelength [30] have been studied. Properly doped BC of $KGd(WO_4)_2$ or $KY(WO_4)_2$ have also been employed as

active elements within a cavity for realizing conical diffraction lasers with specific polarization properties [31–35].

Some of the biaxial crystals giving rise to CD also show another nonlinear optical effect, the photorefractive effect [36]. This is an indirect effect leading to refractive index changes already upon low power light illumination. In this work we combine conical diffraction with photorefraction within the same medium to demonstrate conical diffraction holograms as well as the selective amplification of the CD wave via dynamic two-wave mixing. Section 2 describes briefly the experimental approach and the $Sn_2P_2S_6$ (SPS) crystal used both as medium giving rise to CD and as nonlinear holographic recording material. Section 3 illustrates the major experimental results showing that propagation of the object wave along one of the optical axes of the BC is crucial and critical. Indeed, provided that the object wave propagates along the optical axis and gives rise to CD, holographic recording and two-wave mixing amplification can be efficiently achieved with any combination of the polarizations of the object and reference waves, including mutually orthogonal ones. The underlying physical phenomenon is highly complex and involves the physics of the photorefractive effect in strongly anisotropic configurations as well as the constraints associated to the propagation of light in singular directions within the BC. While a complete theory would require the knowledge of several still unknown material parameters, it is possible to qualitatively catch the main experimental features with a simplified model which is presented and discussed in Sect. 4. Finally, Sect. 5 gives brief remarks and conclusions.

2. Crystal sample and experimental approach

The BC used for the investigations is a nominally undoped ferroelectric SPS, which belongs to the monoclinic point group *m* at room temperature. SPS is an attractive nonlinear optical material owing to its transparency range extending from 530 to 8000 nm wavelength, its interesting electro-optical [37, 38] and nonlinear optical properties [39] and the high photorefractive sensitivity [40, 41]. The anisotropic optical properties and their dispersion were studied in detail in [42] and optical activity near the ferroelectric-paraelectric phase transition was evidenced in [43]. A summary of some of the most relevant material parameters is given in Ref. [41]. A 11.2 mm-long SPS sample was cut from a crystal grown by the vapor transport method [44] and electrically polarized to insure a ferroelectric monodomain state. The sample was oriented with the parallel beam entrance and exit faces being nearly perpendicular to one of the two optic axes.

A simplified scheme of the experimental arrangement for holographic recording and two-wave mixing is shown in Fig. 1. Figure 1(a) is for the holographic recording and read-out of the CD beam created in-situ by the object wave. A He-Ne laser beam at the wavelength of 632.8 nm is split into a reference and an object wave by taking care that the path lengths difference is within the coherence length of the laser. Their polarizations are initially left and right circular, respectively. Before each wave reaches the SPS crystal, the polarizations can be individually modified by polarization controllers (Pol-contr) in each path being composed of linear polarizers, wave-plates or adjustable liquid crystal retarders. The Gaussian input waves have initially an equal diameter and are focused by the spherical lenses L_1 (focal length $f = 200$ mm) and L_2 ($f = 75$ mm) towards the SPS crystal, where they interfere. The positions of the lenses are chosen in such a way that the reference wave has a slightly larger diameter than the object wave inside the crystal (≈ 2.1 mm vs. 1.5 mm). The focal plane of lens L_2 corresponds to the focal image plane where the CD ring pattern formed by the object wave is the sharpest. The spherical lens L_3 images this plane onto a CCD camera to observe the transmitted, amplified or reconstructed CD object wave with the corresponding power being detected in parallel by a photodiode. For holographic recording (but not for two-wave mixing) the input powers of the two beams are adjusted in such a way that the reference and object waves have nearly the same intensity inside the SPS crystal ($I \approx 30$ mW/cm^2). For holographic recording (Fig. 1(a)) shutter S_1 on the object wave is kept open during 90 seconds. This allows to record a photorefractive grating composed

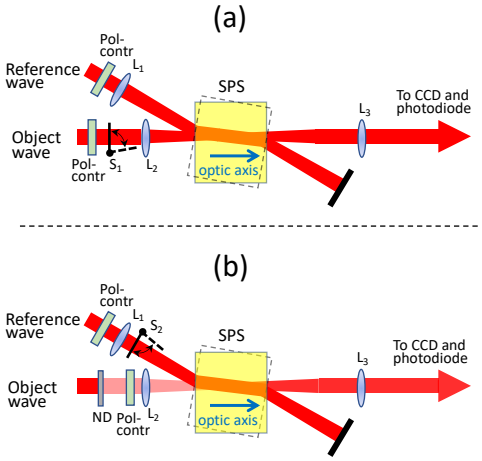

Fig. 1. Scheme of experimental arrangement for the holographic recording and read-out of the CD object wave (a) and for its amplification by two-wave mixing (b). SPS: $Sn_2P_2S_6$ biaxial crystal; S_1, S_2: shutters; L_1, L_2, L_3: spherical lenses; Pol-contr.: polarization controller; ND: neutral density filter. The optic axis of the SPS crystal is aligned with the object wave (yellow shape). The dashed shape give an alternative (misaligned) crystal orientation.

of a fast primary grating nearly fully compensated by a slow secondary grating, this behavior is typical for type I nominally undoped SPS crystals [41]. When the shutter S_1 is being closed, the primary grating disappears quickly revealing the secondary grating that results in the diffraction of the reference wave into the reconstructed object wave. For the examples presented in the next section this reconstructed wave is observed 5 seconds after closing shutter S_1.

The situation for two-wave mixing (Fig. 1(b)) is similar, however with different boundary conditions. Here the object wave is first attenuated by a neutral density filter (ND) to an intensity less than 1/100 (inside the BC) with respect to the one of the reference. In this case, injection of the reference wave by opening shutter S_2 leads to an amplification (or eventual depletion) of the CD object wave. Importantly, we recall that the object wave produces the CD vector beams only if it propagates along the optic axis (yellow orientation of SPS in Fig. 1). By misaligning the crystal (dashed orientation) CD no longer occurs and the behavior differs strongly, as discussed in the next section. In our experiments the horizontal laboratory plane is spanned by the optic axis of the crystal and by the x crystallo-physical axis of the orthogonal Cartesian system used to describe the tensorial properties of SPS. The convention taken is the same one as in Ref. [42] (see Fig. 1 therein), the x-axis is close to the crystallographic a-axis of the monoclinic SPS and to the direction of the spontaneous polarization. The examples given below are obtained for an external crossing angle of 31° between the two waves, what corresponds to a spatial grating period of $\Lambda \approx 1.2$ μm, however other crossing angles give qualitatively similar results.

3. Experiments

As mentioned above, propagation along the optical axis leads to spreading of different linear polarizations across the CD ring pattern. If the input wave is circularly polarized, all the linear polarizations are equally important and the circular ring pattern is homogeneous in intensity. The polarization spreading can be easily visualized by filtering the output CD ring with a linear polarization analyzer placed before the observation CCD camera. This is shown in Fig. 2 which gives the transmitted CD object wave (with no reference wave) for circularly polarized input after

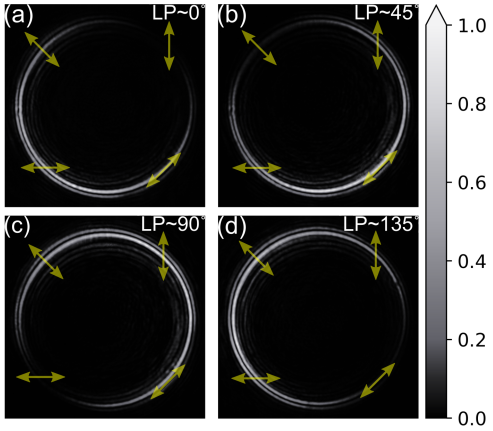

Fig. 2. Polarization-filtered object wave with a linear polarizer (LP) placed before the CCD camera and oriented in four different directions, i.e. (a) 0°, (b) 45°, (c) 90° and (d) 135°. The input object wave is circularly polarized. The nodes in the intensity distribution correspond to the positions where the local polarization in the output CD ring is perpendicular to the LP transmission direction. The arrows give the corresponding local linear polarization directions. The grayscale bar gives the relative intensity scale.

filtering with a polarization analyzer (LP) oriented at 0°, 45°, 90° or 135° in the laboratory frame. Clearly, upon filtering the local intensity depends on the azimuthal position on the ring because the locally transmitted intensity depends quadratically on the projection of the local polarization on the analyzer transmission axis. The positions of the nodes in Fig. 2(a)-(d) correspond thus to the azimuthal positions where the local polarization is perpendicular to the analyzer axis. It can be easily recognized that axially opposite points on the ring are associated to mutually orthogonal local polarizations, as generally expected in the case of CD. It is worth noticing that using a linearly rather than circularly polarized input, that is placing the linear polarizer before rather than after the BC, leads to the same type of crescent-like pattern as in Fig. 2, the full ring being obtained only if the input wave is polarized circularly. The above-discussed azimuthal polarization spreading is a remarkable property of the CD wave in view of the ability to record photorefractive holograms with any combinations of the input beam polarizations. It is indeed always possible to find ring sections of the object wave where the local polarization is such as to produce strong interference with a uniformly polarized reference wave.

We illustrate first this mutual polarization versatility in the case of dynamic two-wave mixing (TWM). This is shown in Fig. 3 which represents the temporal build-up of the spatially integrated object wave amplification $\bar{\gamma}_0$ for various polarizations of the reference wave acting as a pump and a unique polarization of the object wave. The quantity $\bar{\gamma}_0$ is defined as the object wave total power in presence of the reference pump wave divided by the transmitted object wave power without the reference wave. For Fig. 3 the incident object wave is aligned to the optic axis of the BC and is kept right circularly polarized (RCP) while the reference wave polarization is either left circular (LCP) or linear at +45° or -45°. Clearly, upon injection of the reference wave at $t = 0$ [opening of shutter S_2 in Fig. 1(b)], a significant amplification is observed for all polarization combinations, including the case where the two incident waves are mutually orthogonal (RCP and LCP). The amount of amplification differs slightly for the three cases as the strength of the underlying photorefractive gratings and the electro-optic coupling is a function of the wave polarizations. The dynamics seen in Fig. 3 shows the rise of the primary photorefractive grating in a time of the order of one second. Here the maximum of $\bar{\gamma}_0$ does not correspond to a

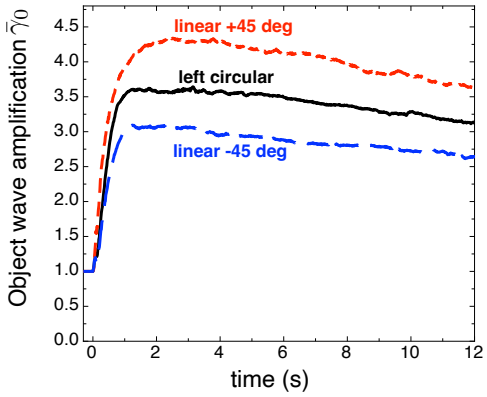

Fig. 3. Two-wave mixing amplification of the object wave as a function of time. The input object wave is aligned to the crystal optic axis and is right circularly polarized. Results for three different polarizations of the incident pumping reference wave are shown: left circular polarization (solid black curve), linear polarization (LP) at +45° (red dashed curve) and LP at -45° (blue dashed curve).

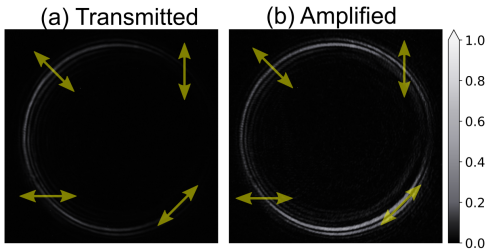

Fig. 4. Two-wave mixing amplification for interfering linearly polarized orthogonal eigenwaves. (a) Transmitted CD object wave in absence of the reference pump wave. (b) Amplified CD object wave. The arrows give the local linear polarization directions at the output and the grayscale bar gives the relative intensity scale.

steady-state because, as mentioned above, for type I SPS crystals a secondary grating starts to compensate the primary one, resulting in the slight decrease of the amplification seen after the maximum. This compensation would be nearly complete after a time of $\approx$ 100 s. It is worth noting that the amplification $\bar{\gamma}_0$ shown in Fig. 3 is an average amplification over the CD ring as obtained by integrating all the power in the object wave using a photodiode. In reality the amplification differs for different sections of the ring, that correspond to different local linear polarizations of the CD wave. This point will be discussed below in connection with Fig. 4. Finally, we would like to point out that larger amplifications than those shown in Fig. 3 are possible for situations where the two input waves share a same polarization. This is the usual condition under which photorefractive two-wave mixing experiments are normally performed. By choosing a reference wave polarization corresponding to one of the two eigenwaves in SPS and the corresponding nearly parallel linear polarization for the input object wave, we have observed in separated experiments a maximum amplification $\bar{\gamma}_0 \approx 10.2$, as compared to a maximum of $\bar{\gamma}_0 \approx 4.3$ in Fig. 3.

As mentioned above, the TWM amplification differs locally, what can be easily seen in Fig. 4. Here the reference wave polarization is linear and corresponds to one of the eigenpolarizations in the SPS crystal. The polarization of the object wave is linear too but is associated to the other (orthogonal) eigenpolarization when the crystal is slightly misaligned. Figure 4(a) shows the

transmitted object wave for the aligned configuration in absence of the reference beam (shutter S_2 in Fig. 1(b) closed). As expected, the observed CD ring pattern is inhomogeneous in intensity as a result of the linear input polarization. After amplification (Fig. 4(b), three seconds after opening shutter S_2) one observes in this specific case a much stronger increase of intensity in the regions on the right side of the CD ring, that were initially weaker. The amplification for the left side of the ring is significantly less pronounced, what give rise to a kind of power equalization within the CD ring. Importantly, we have verified that the amplified CD conserves the same polarization distribution than the linearly transmitted one (see Fig. 4) , meaning that the light amplified by the nonlinear process respects the contraints given by the linear properties of the medium. Note also that in the present example the spatially averaged amplification is $\bar{\gamma}_0 \approx 4.5$. It is interesting to compare this value with the one obtained under the same conditions except for the crystal being turned (misaligned) so that the the object wave no longer propagates along an optic axis. In this case the orthogonal eigenwaves prevent the creation of an efficient photorefractive grating. We have checked this case for an internal misalignment of $\approx 6^\circ$, finding that the object wave is essentially unaffected by the pumping with the reference beam, the amplification being less than 12% ($\bar{\gamma}_0 \approx 1.12$).

The same kind of behavior can be observed for grating diffraction at a photorefractive hologram recorded with orthogonal eigenwaves, as for the case of Fig. 4. Figure 5(a) shows the linear transmission of the object wave under CD conditions, while Fig. 5(b) shows the reconstructed CD wave after closing shutter S_1 in Fig. 1(a) at the end of the recording. Clearly, also here a reconstructed CD vector wave (with same local polarization as the transmitted object wave) is being observed despite for the orthogonal eigenwaves associated to the object and reference beams. As for TWM, also here one observes a locally stronger reconstruction on the right side of the ring, corresponding to a region where the transmitted object wave is weaker. Figure 5(c) and (d) are for the case where the crystal is misaligned and the object wave makes an internal angle of about 6° with the optic axis. In this case the object wave experiences double refraction. The latter can be recognized in Fig. 5(c) that shows its transmission through the SPS crystal. Here the saturated left spot corresponds to the transmission of the dominant object eigenwave while the weak spot on the right corresponds to a spurious intensity on the other (orthogonally polarized) eigenwave . If a hologram is recorded with the reference wave on the orthogonal eigenwave, upon read-out one observes merely a weak diffraction at the position of the right spot [Fig. 5(d)]. Under the same conditions used for the aligned configuration, the corresponding diffracted power in direction of the object wave is about 30 times weaker, which confirms the specific importance of propagating the object wave along the optic axis.

The section of the ring which is most strongly reconstructed depends on the input polarization of the reference wave. This is illustrated with the help of Fig. 6, that shows the results of hologram recording and read-out with linear horizontal or vertical polarization (in the laboratory frame) for the reference wave, together with a circular polarized object input wave at recording. Clearly the horizontal (H-pol) and vertical polarized (V-pol) reference lead to predominant revealing of different sections of the CD ring at read-out, as seen in Fig. 6(b) and (c), respectively. The corresponding angular-dependent powers can be best visualized by integrating the intensity across a narrow radial section across the CD ring for different azimutal angles along the ring, what gives the solid red curve (H-pol) and the dotted blue curve (V-pol) in Fig. 6(d). This behavior can be put in relation with the expectations of a simplified theory, as discussed in the next section.

4. Background theory

The detailed explanation of our above observations in connection with CD holography and TWM is a tedious task. It involves on one hand the physics related to the anisotropic optical properties leading to the CD effect and, on the other hand, the complex physics related to the photorefractive effect [36] in such a low symmetry monoclinic crystal. The latter is concerned by

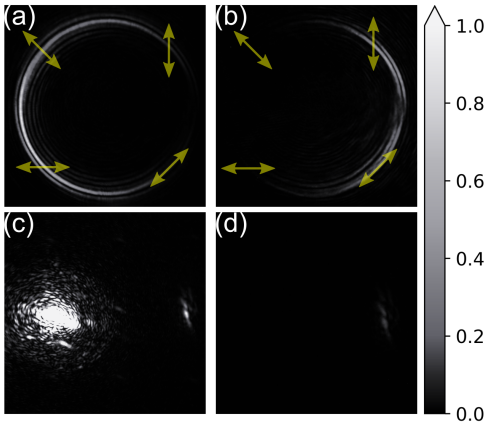

Fig. 5. Holographic recording with orthogonal eigenwaves. Left column: transmitted object wave prior to hologram recording for the aligned (a) and misaligned (c) configurations. Right column: object wave reconstruction at read-out after hologram recording, again for the aligned (b) and misaligned (d) configurations. The arrows in (a) and (b) give the local linear polarization directions for the transmitted and reconstructed object wave, respectively.

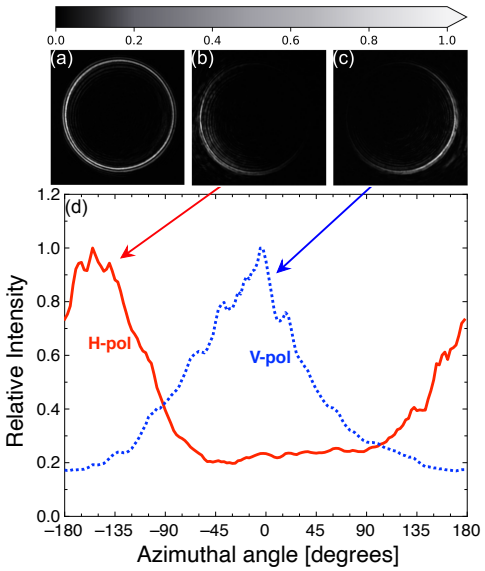

Fig. 6. CD holography with circularly polarized input object wave and linearly polarized (horizontal (H) or vertical (V) in laboratory frame) reference wave. (a) CD object wave transmission prior to hologram recording; (b) Object wave reconstruction for H-polarized reference; (c) Object wave reconstruction for V-polarized reference; (d) Normalized azimuthal dependence of local power on the reconstructed ring for cases (b) and (c).

the photoinduced charge transport leading to the formation of a space-charge field distribution and by its conversion into a refractive index modulation (phase hologram) by means of the material's electro-optic response. However, the space-charge electric field in the case of a photorefractive grating is periodically modulated in space and the electro-optic response gets

an additional level of complexity as compared to the case where the field would be spatially homogeneous. A thorough quantitative description requires the knowledge of all clamped electro-optic coefficients, as well as of all the elastic, elasto-optic and piezo-electric properties of the crystal, a significant part of which is still unknown for SPS. More details on these aspects can be found in [45, 46] and references therein. For the above reasons the purpose of this section is not to find a quantitative agreement between experiments and theory, but rather to confirm the plausibility of the observation in the framework of a highly simplified theoretical approach.

As discussed above in connection with Fig. 2, the local polarization direction on the CD varies along the ring circumference and spans an angle θ of 180° over a full revolution of the polar angle φ by 360°, the variation in θ being always half the variation in φ. Considering different spatial positions on the ring is therefore equivalent to considering a given linear polarization component for the object wave among all the possible ones in the plane perpendicular to the object wave $\vec{k}$-vector. We recall that for a circularly polarized input object beam the different linear polarizations are equally probable , giving thus a complete ring. The easiest situation is the one where the reference wave is linearly polarized (as for instance in Fig. 6). In this case the problem of estimating the azimuthal dependence of the hologram diffraction efficiency and TWM gain reduces essentially to an evaluation of the coupling strengths between a plane reference wave with a fixed polarization and components of the object wave with all possible polarization directions taken as a variable parameter. This coupling strength follows from coupled wave theory for anisotropic gratings [47] and is a function of several material and experimental parameters. On one hand, in the case of a grating created by means of the photorefractive effect the coupling strength depends on the modulation depth amplitude of photorefractive space-charge field created by the two considered wave components. On the other hand it depends on an effective scalar electro-optic coefficient r_{eff} specific to the pair of waves being considered. This coefficient is a function of the unit vector $\widehat{K}$ in the direction of the grating vector, of the anisotropic electro-optic properties expressed by a tensor r^{eff}_{ijk} (see Ref. [45]), and of the two unit polarization vectors $\widehat{d}^{ref}$ and $\widehat{d}^{obj}$ for the reference and object waves, respectively. Importantly, here $\widehat{d}^{obj} \equiv \widehat{d}^{obj}(\theta)$ is the local object wave polarization corresponding to a given azimuthal position on the CD ring. The expression for the scalar electro-optic coefficient determining the coupling is [45]

$$r_{eff} = \widehat{d}^{obj}_i \cdot (r^{eff}_{ijk} \hat{K}_k) \cdot \widehat{d}^{ref}_j \,, \tag{1}$$

where the Einstein summation convention over equal indices is utilized. Importantly, all the vectors in the above equation have to be expressed in the orthogonal crystallo-physical reference frame (xyz) in which the electro-optic tensor and other tensorial physical properties of the crystal are usually expressed. This crystallo-physical system is oblique with respect to the laboratory frame. As an example, the unit vector along the optic axis of propagation of the object wave is expressed in the xyz-system as (0.4678, 0.7660, 0.4408). In the laboratory frame the same vector would possess only a unique unity component along the longitudinal coordinate perpendicular to the entrance surface plane of the crystal. As discussed in [45], the third-rank tensor r^{eff}_{ijk} to be used in in (1) is a function of the clamped (high-frequency) electro-optic tensor elements and depends also on the elastic, piezoelectric and elasto-optic properties of the material. Unfortunately there is a lack of sufficient data on these mechanical properties for SPS, so that we do not have access to the correct values to be used for the coefficients of the tensor r^{eff}_{ijk}. Instead we take a rather rude approximation and we utilize the unclamped (free) electro-optic tensor elements r^{T}_{ijk} that were measured in [37] and [38] for what matters the first and third column of the tensor, respectively. The employed values (in units of pm/V) are: r^{T}_{111}=174, r^{T}_{221}=92, r^{T}_{331}=140, r^{T}_{131}=-25, r^{T}_{113}=-67, r^{T}_{223}=-22, r^{T}_{333}=-25 and r^{T}_{133}=14. The two still unknown coefficients r^{T}_{322} and r^{T}_{122} are expected to be rather small as they are associated to electric field directions perpendicular to the crystallographic mirror plane containing the crystal's spontaneous polarization. Both these

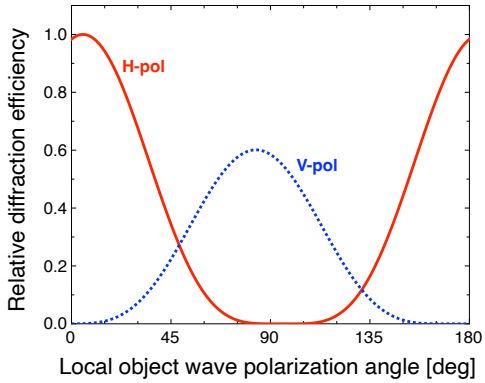

Fig. 7. Expected relative diffraction efficiency based on the simplified model described in Sect. 4. The object input wave is assumed circularly polarized and contain all linear polarization angles between 0° and 180°. The reference wave is assumed horizontally (red solid curve) or vertically polarized in the laboratory frame (blue dotted curve).

coefficients are set equal 0 for the following evaluation. Note also that the third column (index $k = 3$) diagonal coefficients r_{113}, r_{223} and r_{333} are taken here with the opposite sign as in the original publication [38]. The reason is the different convention for the positive direction of the z-crystallo-physical axis. Here we stick to the the convention in Ref. [42] which is consistent with the IEEE Standard on Piezoelectricity [48], with positive x- and z-direction such that both piezoelectric coefficients d_{111} and d_{333} are positive, while in [38] a convention with d_{333} negative was taken. It is also worth mentioning that for our experimental configuration the photorefractive space-charge electric field has the largest projection on the x-axis and the elements of the first column ($k = 1$) of the electro-optic tensor largely determine the resulting scalar electro-optic coefficient of Eq. (1).

The expected local hologram diffraction efficiency η is proportional to the square of the product of r_{eff} with the amplitude E_{sc} of the photorefractive space-charge grating responsible for the coupling of the two waves, i.e. [47]

$$\eta \propto [r_{eff}(\theta) E_{sc}]^2 \quad . \tag{2}$$

This relation is valid for moderate diffraction efficiencies of the phase hologram, what is the case for our gratings where the spatially averaged diffraction efficiency is typically of the order of 2-3 %. For what matters the space-charge field amplitude, we assume here that it is proportional to the light modulation index induced by the two local polarizations, i.e. to the scalar product $E_{sc} \propto (\widehat{d}^{obj} \cdot \widehat{d}^{ref})$. This is a rather rude approximation for various reasons, the principal one being associated to the fact that the space-charge field saturates at large modulation (for nearly parallel $\widehat{d}^{obj}$ and $\widehat{d}^{ref}$), what leads to a sublinear dependence of E_{sc} on the modulation depth in this regime. Therefore, the use of this approximation may lead to an excessive contrast in the simulated curves for η as a function of the object wave polarization angle. Such a simulation is shown in Fig. 7 for the case of a circularly polarized input object wave and a linearly polarized reference (horizontal or vertical), as for the case of Fig. 6. It can be easily recognized in Fig. 7 that the diffraction for the horizontal and vertical polarization of the reference beam are nearly (but not exactly) in anti-phase, meaning that their maxima are separated by approximately 90° in the object wave polarization, what corresponds to 180° on the CD ring. Despite for the many simplifying assumptions, such a behavior agrees qualitatively with the experimental results shown in Fig. 6.

In the case of two-wave mixing with weak signal wave, the local amplification $\gamma(\theta)$ is expected

to depend exponentially on the exponential gain $\Gamma(\theta)$ as [36]

$$\gamma(\theta) = e^{\Gamma(\theta)d} \ , \tag{3}$$

where d is the propagation distance in the crystal. In absence of an anisotropy of the photoexcitation process [46] the exponential gain can be expressed as

$$\Gamma \cong B(\widehat{e}^{obj} \cdot \widehat{e}^{ref}) r_{eff}(\theta) \tilde{E}_{sc,im} \ , \tag{4}$$

where B is a constant that depends on the refractive indices associated to the two waves, on the light wavelength, and on the weak walk-off angle for the reference wave. Here $\tilde{E}_{sc,im}$ is the imaginary part of the space-charge field amplitude. This is the nonlocal component of the space-charge field (90° phase shifted with respect to the intensity modulation) and is responsible for the TWM gain. In materials with diffusion dominated charge transport, as in SPS [41], this is the dominant component of the space-charge field. Importantly, this quantity depends on experimental and materials parameters such as the beams crossing angles, the trap density in the crystal or its static dielectric properties. However, $\tilde{E}_{sc,im}$ does not depend on the relative intensity of the two-waves and the corresponding light modulation depth, so that it can be considered as a constant for our purposes. In (4) the unit vectors $\widehat{e}^{obj}$ and $\widehat{e}^{ref}$ are along the electric fields of the object and reference waves, respectively. Due to the weak walk-off their scalar product can be safely approximated by the corresponding scalar product of the electric displacement unit vectors $\widehat{d}^{obj}$ and $\widehat{d}^{ref}$, so that

$$\Gamma \cong C(\widehat{d}^{obj} \cdot \widehat{d}^{ref}) r_{eff}(\theta) \ , \tag{5}$$

where C is again a constant that depends on the specific experimental arrangement. In this equation the dependence on the local object wave polarization angle θ appears twice, in the effective scalar electro-optic coefficient $r_{eff}(\theta)$ and in the scalar product between the two $\widehat{d}$ vectors. Figure 8 shows the expected amplification of the object wave for the case where the input polarizations of the object and reference wave are linear and mutually orthogonal and the reference wave polarization is aligned to one of the eigenpolarizations. This situation corresponds to the one of Fig. 4. The evaluation follows from the simplifying approach of Eqs. (3), (5) and (1) where the constant C was adjusted to give an average amplification $\bar{\gamma}_0 \approx 4.5$. In Fig. 8 the angle θ is given relative to the input polarization angle $\theta_{0,\mathrm{obj}}$ of the object wave ($\theta_{0,\mathrm{obj}} = -63.2°$), so that the input wave intensity distribution (assumed proportional to $\cos^2(\theta - \theta_{0,\mathrm{obj}})$ is centered on the graph (dashed red curve). It can be recognized that the central region where the object wave has a maximum in absence of TWM interaction (corresponding to the left region in Fig. 4(a)) is not being amplified. This is due to the vanishing scalar product in (5) at this point. The maximum power in the amplified wave is predicted for two regions with a deviation of roughly ±60° in θ (±120° along the ring) from this position. These maxima have different heights and are mainly a result of a combination of the effects of $r_{eff}(\theta)$ together with the initial θ-dependence of the unaffected CD wave. Even though the gain Γ tends to increase when the polarization direction θ gets closer to the one of the reference (at the two borders of the graph in Fig. 8), from a certain point on the lack of input light possessing such polarization components becomes dominant, what gives the minimum at ±90° in Fig. 8. Experimentally this minimum corresponds to the dark region on the right-hand side of the circle on Fig. 4(b). Again, despite the highly simplifying assumptions, one can conclude that our modeling gives a satisfactory qualitative agreement with the observations. It is also worth mentioning that, even though here the average amplification is only slightly more than a factor of 4, locally the light can be amplified much stronger with peaks exceeding a factor of 40.

5. Discussion and conclusion

We have considered conical diffraction vector waves in a nonlinear photorefractive and optically biaxial material and we have shown, for the first time to our knowledge, that it is possible

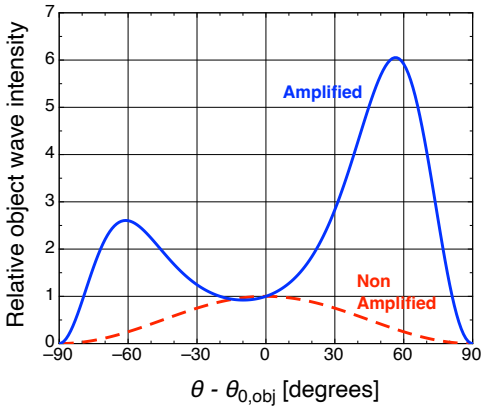

Fig. 8. Expected TWM amplification of the CD object wave as a function of the local angle of polarization θ for the case of orthogonal linearly polarized input waves with the reference wave as one of the eigenpolarizations. The angle $\theta_{0,\mathrm{obj}}$ is the polarization angle of the input object wave, for which the non amplified CD wave is locally maximum. Red dashed curve: non amplified wave; Blue solid curve: amplified object wave with $\bar{\gamma}_0 \approx 4.5$.

to amplify locally or record in-situ holograms of such waves. The biaxial crystal acts both as generator of the CD vector wave and as a recording material. The holographic recording process possesses a kind of angular resonance for the object wave direction parallel to one of the optical axes. It was shown that under these aligned CD conditions of the crystal the recording is possible even for orthogonal polarizations of the two interacting input beams thanks to the polarization spreading resulting from the CD process. This property is remarkable since the hologram recording is driven by the intensity distribution, as in conventional holography, and not by the polarization states of the interacting waves, as in the framework of polarization holography in polarization-sensitive media [49]. It was found that the pattern reconstruction depends on the combination of recording polarizations and on the read-out polarization. For two-wave mixing we obtain a varying local amplification across the CD ring, which can partially lead to a more homogeneous power around the circle. The observed effects could be used as an additional way to dynamically control the structure of the CD ring beam, for instance in connection to optical particle trapping. We have analyzed the situation with the help of a highly simplified theoretical approach based on the model of the photorefractive effect and general features of conical diffraction. Despite its simplicity and the number of assumptions, the model allows a surprisingly good qualitative description of the main experimental features. A more thorough modeling would require the determination of a number of still unknown anisotropic material parameters, as well as the consideration of details regarding CD under the conditions of optical activity [50,51], which is little investigated to date and was neglected for the purpose of this work. The present investigations have dealt with CD in a single crystal without cascades. However, more complex vector patterns can be obtained with CD cascades, up to the cases where their circularly symmetry is being broken [16,17]. Since in such cases the output patterns are obtained in the last focal image plane (near the last crystal in the cascade), we expect that recording and local amplifications of such more complex patterns shall be possible as well if this last crystal is able to store a hologram.

Acknowledgments. This research work was funded by the Lorraine Université d'Excellence (LUE) initiative and by the French-Ukrainian bilateral PHC DNIPRO program.

Disclosures. The authors declare no conflicts of interest.

Data Availability. Data underlying the results presented in this paper are not publicly available at this time but may be obtained from the authors upon reasonable request.

References

1. M. V. Berry, "Conical diffraction asymptotics: fine structure of Poggendorff rings and axial spike," J. Opt. A: Pure Appl. Opt. **6**, 289–300 (2004).
2. M. V. Berry, M. R. Jeffrey, and J. G. Lunney, "Conical diffraction: observations and theory," Proc. R. Soc. A: Math. Phys. Eng. Sci. **462**, 1629–1642 (2006).
3. A. Turpin, Y. V. Loiko, T. K. Kalkandjiev, and J. Mompart, "Conical refraction: fundamentals and applications," Laser Photonics Rev. **10**, 750–771 (2016).
4. W. R. Hamilton, "Third supplement to an essay on the theory of systems of rays," Trans. Royal Ir. Acad. **17**, 1–144 (1837).
5. A. M. Belskii and A. P. Khapalyuk, "Internal conical refraction of bounded light beams in biaxial crystals," Opt. Spectrosc. **44**, 436–439 (1978).
6. M. V. Berry, M. R. Jeffrey, and M. Mansuripur, "Orbital and spin angular momentum in conical diffraction," J. Opt. A: Pure Appl. Opt. **7**, 685 (2005).
7. D. P. O'Dwyer, C. F. Phelan, Y. P. Rakovich, P. R. Eastham, J. G. Lunney, and J. F. Donegan, "Generation of continuously tunable fractional optical orbital angular momentum using internal conical diffraction," Opt. Express **18**, 16480–16485 (2010).
8. A. Brenier, A. Majchrowski, and E. Michalski, "Light propagation properties of the $Bi_2ZnOB_2O_6$ acentric biaxial crystal: Angular orbital momentum from conical diffraction," Opt. Mater. **91**, 286–291 (2019).
9. X. Sun, Y. Geng, Q. Zhu, W. Huang, Y. Zhang, W. Wang, and L. Liu, "Unitary transformation for Poincaré beams on different parts of Poincaré sphere," Sci. Rep. **10**, 1–10 (2020).
10. A. Brenier, "Evolution of vortices created by conical diffraction in biaxial crystals versus orbital angular momentum," Opt. Mater. **110**, 110504 (2020).
11. M. V. Berry, "Conical diffraction from an N-crystal cascade," J. Opt. **12**, 075704 (2010).
12. C. F. Phelan, K. E. Ballantine, P. R. Eastham, J. F. Donegan, and J. G. Lunney, "Conical diffraction of a Gaussian beam with a two crystal cascade," Opt. Express **20**, 13201–13207 (2012).
13. A. Turpin, Y. V. Loiko, T. K. Kalkandjiev, and J. Mompart, "Multiple rings formation in cascaded conical refraction," Opt. Lett. **38**, 1455–1457 (2013).
14. V. Peet, "Variable two-crystal cascade for conical refraction," Opt. Lett. **40**, 2405–2408 (2015).
15. S. Mohammadou, B. Mohamadou, and G. Montemezzani, "Complex beam shaping by cascaded conical diffraction with intercalated polarization transforming elements," Opt. Express **25**, 25392–25406 (2017).
16. M. W. Iqbal, N. Marsal, and G. Montemezzani, "Non-circularly shaped conical diffraction," Sci. Rep. **12**, 7317 (2022).
17. M. W. Iqbal, N. Marsal, and G. Montemezzani, "Shape and polarization distribution of non-circular conical diffraction beams from conjugate cascades," Opt. Express **31**, 29859–29876 (2023).
18. D. P. O'Dwyer, K. E. Ballantine, C. F. Phelan, J. G. Lunney, and J. F. Donegan, "Optical trapping using cascade conical refraction of light," Opt. Express **20**, 21119–21125 (2012).
19. A. Turpin, J. Polo, Y. V. Loiko, J. Küber, F. Schmaltz, T. K. Kalkandjiev, V. Ahufinger, G. Birkl, and J. Mompart, "Blue-detuned optical ring trap for Bose-Einstein condensates based on conical refraction," Opt. Express **23**, 1638–1650 (2015).
20. D. Pfeiffer, L. Lind, J. Küber, F. Schmaltz, A. Turpin, V. Ahufinger, J. Mompart, and G. Birkl, "Trapping of bose-einstein condensates in a three-dimensional dark focus generated by conical refraction," Phys. Rev. A **108**, 053320 (2023).
21. A. Turpin, Y. Loiko, T. K. Kalkandjiev, and J. Mompart, "Free-space optical polarization demultiplexing and multiplexing by means of conical refraction," Opt. Lett. **37**, 4197–4199 (2012).
22. V. Peet, "Biaxial crystal as a versatile mode converter," J. Opt. **12**, 095706 (2010).
23. T. Novikova et al., "Metrology of replicated diffractive optics with Mueller polarimetry in conical diffraction," Opt. Express **15**, 2033–2046 (2007).
24. A. Peinado, A. Lizana, A. Turpín, C. Iemmi, T. K. Kalkandjiev, J. Mompart, and J. Campos, "Optimization, tolerance analysis and implementation of a Stokes polarimeter based on the conical refraction phenomenon," Opt. Express **23**, 5636–5652 (2015).
25. S. Rosen, G. Y. Sirat, H. Ilan, and A. J. Agranat, "A sub wavelength localization scheme in optical imaging using conical diffraction," Opt. Express **21**, 10133–10138 (2013).
26. J. Caron, C. Fallet, J.-Y. Tinevez, L. Moisan, L. P. Braitbart, G. Y. Sirat, and S. L. Shorte, "Conical diffraction illumination opens the way for low phototoxicity super-resolution imaging," Cell Adhes. Migr. **8**, 430–439 (2014).
27. J. Kroupa, "Second-harmonic conical refraction in GUHP," J. Opt. **12**, 045706 (2010).
28. V. Peet and S. Shchemelyov, "Frequency doubling with laser beams transformed by conical refraction in a biaxial crystal," J. Opt. **13**, 055205 (2011).
29. S. D. Grant, S. A. Zolotovskaya, T. K. Kalkandjiev, W. A. Gillespie, and A. Abdolvand, "On the frequency-doubled conically-refracted Gaussian beam," Opt. Express **22**, 21347–21353 (2014).

30. J. Ma, P. Yuan, J. Wang, G. Xie, H. Zhu, and L. Qian, "Sum-frequency generation with femtosecond conical refraction pulses," Opt. Lett. **43**, 3670–3673 (2018).
31. J. Hellström, H. Henricsson, V. Pasiskevicius, U. Bünting, and D. Haussmann, "Polarization-tunable Yb: KGW laser based on internal conical refraction," Opt. Lett. **32**, 2783–2785 (2007).
32. A. Abdolvand, K. G. Wilcox, T. K. Kalkandjiev, and E. U. Rafailov, "Conical refraction Nd:$KGd(WO_4)_2$ laser," Opt. Express **18**, 2753–2759 (2010).
33. K. Wilcox, A. Abdolvand, T. Kalkandjiev, and E. Rafailov, "Laser with simultaneous Gaussian and conical refraction outputs," Appl. Phys. B **99**, 619–622 (2010).
34. R. Cattoor, I. Manek-Hönninger, D. Rytz, L. Canioni, and M. Eichhorn, "Laser action along and near the optic axis of a Holmium-doped $KY(WO_4)_2$ crystal," Opt. Lett. **39**, 6407–6410 (2014).
35. A. Brenier, "Lasing with conical diffraction feature in the $KGd(WO_4)_2$:Nd biaxial crystal," Appl. Phys. B **122**, 237 (2016).
36. P. Günter and J.-P. Huignard, eds., *Photorefractive Materials and Their Applications, Vol. 1: Basic Effects* (Springer, 2006).
37. D. Haertle, G. Caimi, A. Haldi, G. Montemezzani, P. Günter, A. A. Grabar, I. Stoika, and Y. M. Vysochanskii, "Electro-optical properties of $Sn_2P_2S_6$," Opt. Commun. **215**, 333–343 (2003).
38. G. Montemezzani, M. Aillerie, X. Zheng, H. Remmach, and A. A. Grabar, "Third column electro-optical coefficients of monoclinic $Sn_2P_2S_6$," Opt. Mater. Express **2**, 920–928 (2012).
39. D. Haertle, M. Jazbinšek, G. Montemezzani, and P. Günter, "Nonlinear optical coefficients and phase-matching conditions in $Sn_2P_2S_6$," Opt. Express **13**, 3765–3776 (2005).
40. S. G. Odoulov, A. N. Shumelyuk, U. Hellwig, R. A. Rupp, and A. A. Grabar, "Photorefractive beam coupling in tin hypothiodiphosphate in the near infrared," Opt. Lett. **21**, 752–754 (1996).
41. A. A. Grabar, M. Jazbinšek, A. N. Shumelyuk, Y. M. Vysochanskii, G. Montemezzani, and P. Günter, *Photorefractive Effects in $Sn_2P_2S_6$* (Springer, New York, 2007), pp. 327–362.
42. D. Haertle, A. Guarino, J. Hajfler, G. Montemezzani, and P. Günter, "Refractive indices of $Sn_2P_2S_6$ at visible and infrared wavelengths," Opt. Express **13**, 2047–2057 (2005).
43. R. Vlokh, O. Mys, A. Grabar, and Y. Vysochanskii, "Optical activity of $Sn_2P_2S_6$ crystals at the phase transition," Ukr. J. Phys. Opt **9**, 1–9 (2008).
44. C. Carpentier and R. Nitsche, "Vapour growth and crystal data of the thio(seleno)-hypodiphosphates $Sn_2P_2S_6$, $Sn_2P_2Se_6$, $Pb_2P_2Se_6$ and their mixed crystals," Mater. Res. Bull. **9**, 401–410 (1974).
45. G. Montemezzani and M. Zgonik, *Space-charge driven holograms in anisotropic media* (Springer, New York, 2006), pp. 83–118.
46. G. Montemezzani, "Optimization of photorefractive two-wave mixing by accounting for material anisotropies: $KNbO_3$ and $BaTiO_3$," Phys. Rev. A **62**, 053803 (2000).
47. G. Montemezzani and M. Zgonik, "Light diffraction at mixed phase and absorption gratings in anisotropic media for arbitrary geometries," Phys. Rev. E **55**, 1035 (1997).
48. "IEEE Standard on Piezoelectricity," ANSI/IEEE Std 176-1987 p. 242 (1988).
49. J. Wang, X. Tan, P. Qi, C. Wu, L. Huang, X. Xu, Z. Huang, L. Zhu, Y. Zhang, X. Lin, J. Zang, and K. Kuroda, "Linear polarization holography," Opto-Electron. Sci. **1**, 210009 (2022).
50. A. Belsky and M. Stepanov, "Internal conical refraction of light beams in biaxial gyrotropic crystals," Opt. Commun. **204**, 1–6 (2002).
51. A. Brenier, A. Majchrowski, and E. Michalski, "Phase distributions accompanying the conical diffraction through a Pasteur acentric biaxial crystal, displayed with $Bi_2ZnOB_2O_6$," Opt. Mater. **128**, 112353 (2022).